

ORIGINAL ARTICLE

The restored opus sectile panel from the luxurious episcopal residence in the ancient city of Stobi—mineralogical and chemical findings

Petre Makreski¹  | Tena Šijakova-Ivanova² | Zoran Georgiev³ | Dafinka Balabanova Aleksova³ | Arianit A. Reka^{4,5}  | Blazo Boev² | Gligor Jovanovski⁶

¹Institute of Chemistry, Faculty of Natural Sciences and Mathematics, Ss. Cyril and Methodius University in Skopje, Skopje, Republic of North Macedonia

²Faculty of Natural and Technical Sciences, Goce Delčev University, Štip, Republic of North Macedonia

³National Conservation Centre, Skopje, Republic of North Macedonia

⁴Department of Chemistry, Faculty of Natural Sciences and Mathematics, University of Tetovo, Tetovo, Republic of North Macedonia

⁵Department of Materials Science and Engineering, Missouri University of Science and Technology, Rolla, MO, USA

⁶Research Center for Environment and Materials, Macedonian Academy of Sciences and Arts, Skopje, Republic of North Macedonia

Correspondence

Petre Makreski, Institute of Chemistry, Faculty of Natural Sciences and Mathematics, Ss. Cyril and Methodius University in Skopje, Arhimedova 5, 1000 Skopje, Republic of North Macedonia.

Email: petremak@pmf.ukim.mk

Abstract

Samples from the opus sectile panel excavated from the Episcopal Residence building at the archaeological site of Stobi were examined using X-ray powder diffraction, SEM-EDS, and Raman spectroscopy. The analyzed samples, exhibiting plentiful color and surface variations, comprise the reconstructed sectile panel as well as represent the in situ ground remains. The complementary techniques revealed dominant amorphous phase in five samples, whereas the remaining seven specimens confirmed the presence of magnesite, quartz, dolomite, ankerite, cuprite, wüstite, and hematite. The work represents the first systematic attempt to determine the mineral phases in the restored opus sectile panel, assembled by decorative minerals forming a geometric net of polychrome crosses. Furthermore, the mineral characterization has revealed an origin of mineral species not typical for Macedonian terrain (ankerite, wüstite, cuprite, transparent quartz) that lead to the conclusion that the samples were likely imported from other early-Christian communities.

KEYWORDS

archaeometry, episcopal residence, minerals, North Macedonia, opus sectile panel, Stobi

INTRODUCTION

Stobi was an ancient town of Paeonia established in the Archaic period. Later, under Augustus' reign, it was transformed into the capital for the entire Roman province of Macedonia Salutaris (Roisman

& Worthington, 2010). The town of Stobi covered an area of 25,000 square meters and was major a strategic, merchant, and military center. The name *Stobi* is a Paeonian word meaning “post, pillar” (Katičić, 1976).

The samples that are the subject of analysis were selected from a religious relic within the luxurious Episcopal Residence. The relic was a panel made using the mosaic technique *opus sectile* discovered in 2004. The building (fourth–sixth century AD) at first was thought to be a Casino after the discovery of a bronze dish used for table games (*tabula lusoriae*) (Mano-Zissi, 1973; Wiseman, 1973; Wiseman, 2007). The excavation of this building began in October 1940 (Mano Zissi, 1940) and continued from 2001 to 2009, showing that this was an early-Christian residence of the bishops of Stobi.

Within an inconspicuous utility room of the residence (no.16), situated next to the main apsidal hall of the building, charred remains of wooden panels were discovered in the layer of fire, luxuriously decorated with refined multicolored minerals applied to a wooden base with the mosaic technique *opus sectile*. The minerals were carved into different forms: squares, rectangles, rhombuses, triangles, polygons, and curvilinear shapes, with dimensions from 3.6 to 60 mm (Figure S1, Supplementary Material). All mosaic pieces, almost 3,500, have glossy polished obverse sides. After the base burnt, the mosaic pieces moved, but they kept their general placement in horizontal and vertical rows, and one uncharred and relatively intact edge of the panel enables one to deduce the pattern. The mosaic pattern consists of crossed thin and thick lines, divided into squares and rectangles that create a geometric network of polychrome crosses (and crosses within crosses), connected in horizontal, vertical and diagonal directions (Georgiev, 2018) (Figure S2, Supplementary Material). According to preliminary laboratory examinations, a glue of colophony resin (Robeva-Čukovska et al., 2008–2009) was used to apply the minerals, which burned along with the wooden base and removed the golden foil from the crystals in doing so.

The artistic style of the decoration points to a Levant–Eastern Mediterranean provenance of the charred object. Most likely, it was made in one of the large early Christian centres that were in the circle of influence of Antiochian art (Georgiev, 2018). This conclusion was also confirmed with the only identical find, known recently in archaeological science as “The Golden Sectile” from Caesarea Maritima in Israel (Herod's and biblical Caesarea, Palestinian-Syrian) (Gorin-Rosen, 2015). In comparison to the find in Stobi, this archaeological find, discovered in 2005 and affirmed as “unique in the world” (Gorin-Rosen, 2015), is characterized by simpler craftsmanship, modest presence of Christian symbols and far lower value materials (cast glass tiles with cross and rosette reliefs, laminated in gold foil). Nevertheless, the concept and technical approach are entirely the same as those of the sectile from Stobi (Georgiev, 2018).

The selection of minerals used in the production of the sectile is not random but reflects religious consistency. Namely, it was a church relic that contained holy remains of a Christian martyr, whose original place was in the martyrrium with representative crypt and deambulatorium in the cathedral (Basilica of Bishop Phillip) (Georgiev, 2018). Hence, the completion of the first of two construction phases of the church, which dates to the first half of the fifth century (Aleksova, 1985; Aleksova, 1997; Wiseman, 1973), is also the latest date for construction and delivery of the relic, with a certain possibility for slightly earlier dating, in the last decades of the fourth century (Aleksova, 1997; Mano-Zissi, 1973; Wiseman, 1973). Toward the end of the sixth century, imminently before the attack of the Avars and the Slavs, this holy religious relic and most precious inventory was hidden in the utility room of the bishop's residence, where it was charred during the fire (Georgiev, 2018).

Although a random analysis of some mineralogical samples from Stobi was undertaken by means of X-ray powder diffraction (Boev et al., 2008), this work aims to systematically evaluate and determine, in terms of chemical and mineralogical evaluation, the pieces excavated from the Episcopal Residence building that assemble the *opus sectile* panel (Figure S2, Supplementary Material). For such purpose, three complementary analytical and structural techniques, each with their own advantages and limitations (X-ray powder diffraction, SEM-EDS and Raman spectroscopy), were used. Therefore, the purpose of the work also aims to uncover the eventual domestic origin of the pieces,

or whether their existence resulted from a technological transfer or trading activities. In addition, a detailed approach was carried out to identify the nature of the glassy samples and to correlate their chemical composition with the obtained polymerization index (intensity ratio of the A_{500}/A_{1000} bands) extracted from the Raman spectra (Colomban, 2003).

MATERIALS AND METHODS

The 12 tested samples excavated from the Episcopal Residence at Stobi archaeological site exhibit various colors due to their different chemical compositions. Figure 1 (top panel) combines the macro-photographs of the analyzed samples and their morphological features. Seven of these 12 samples, on the basis of their morphological similarities, were selections from the geometric network

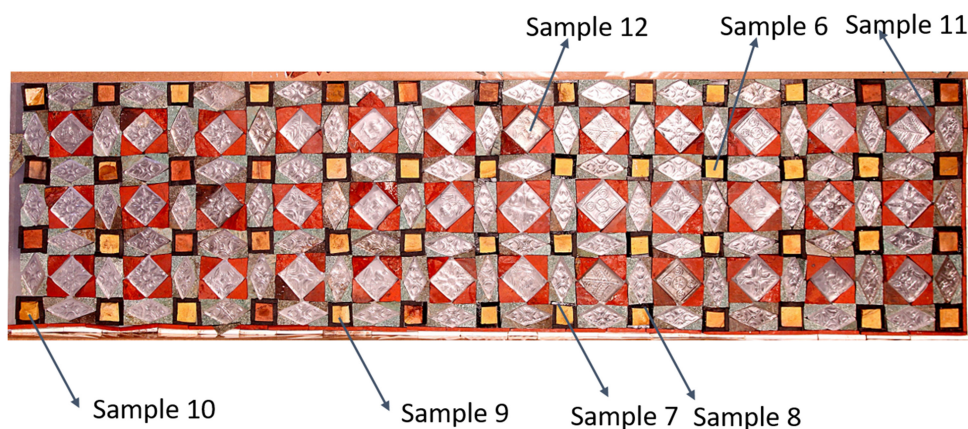
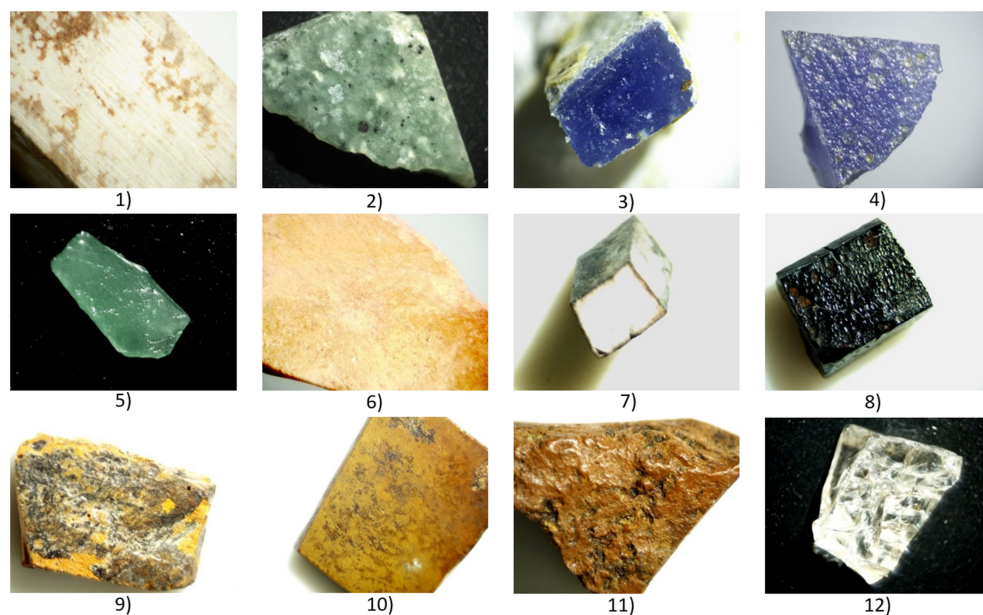


FIGURE 1 Photographs of 12 different samples excavated in the Episcopal Residence at the archaeological site Stobi (top) *Notes:* Samples 6–12 correspond to the specimens that assemble the opus sectile panel (bottom). [Color figure can be viewed at wileyonlinelibrary.com]

of the restored sectile panel (denoted sample 6 to 12, Figure 1 bottom panel), whereas the first five samples were taken from the in situ sectile finding (denoted sample 1 to 5). These five samples were differently colored and exhibit rather diverse surface features in contrast to the previously mentioned seven pieces from the sectile panel.

Early methods of studying archeological materials started with microscopic observations and measurements of physical properties like color, density, hardness, and refractive index. Later, microscopic examination implemented different lighting conditions using natural, polarized, and cross-polarized light. Over the past 50 years, various analytical methods and instrumentation have been successfully employed in archaeological studies on many materials (e.g. elemental analysis, atomic spectrometry, X-ray fluorescence, X-ray diffraction, structural analysis, mass spectrometry, Raman spectroscopy, FTIR spectroscopy, scanning electron microscopy-energy dispersive spectroscopy; thermal analysis, electron spin resonance, isotope analysis, etc.) (Ciliberto & Spoto, 2000; Tykot, 2004).

The study of the collected samples from the Episcopal Residence at Stobi were performed using techniques available to us that were also complementary, modern, and very frequently used in the archeological studies: scanning electron microscopy-energy dispersive spectrometry (SEM-EDS), X-ray powder diffraction (XRPD), and Raman spectroscopy. In addition to the well-known advantages of the former two techniques (Raman: highly specific like a chemical fingerprint of a material; volume smaller than 1 μm in diameter of needed sample; short time of their requirement; covering of the 4,000 cm^{-1} to 50 cm^{-1} region by a single recording; and so on; SEM-EDS: providing digital image resolution as low as 15 nm; enabling coating thicknesses and grain size determinations; providing qualitative elemental analysis and standardless quantitative analysis; etc.), one of the most prominent advantage of these two techniques is their nondestructive nature (Beran & Libowitzky, 2004; Chen et al., 2015; Choudhary & Choudhary, 2017; McMillian & Hofmeister, 1988). On the other hand, the XRPD is known as a destructive technique that requires preparation of a minimal sample for analysis. In spite of that, it is a rapid and powerful technique for identifying unknown materials (minerals), and the resulting data are relatively straightforward to interpret (Kimmel & Mogilyanski, 2009). It should be taken into account, however, that portable X-ray powder diffractometers for the nondestructive analysis of art and archeological materials have been developed during the last decade (Nakai & Abe, 2012). One of the disadvantages of Raman spectroscopy is the appearance of fluorescence from the sample itself or from incorporated impurities. Also, in some cases, the intense laser radiation can destroy the sample and consequently change the real spectral appearance. In scanning electron microscopy, samples that are strong insulators must be coated (usually with gold or carbon) before imaging. This process can result in artifacts and consequently it may affect results (Juhász et al., 2021).

Quantitative SEM-EDS analysis was performed using a TESCAN VEGA3 LMU (Tescan, Czech Republic) scanning electron microscope. It is equipped with an EDS INCA Energy 250XT system (Oxford instruments, UK). The following standards were used: O – SiO_2 ; Na – albite; Mg – MgO ; Al – Al_2O_3 ; Si – SiO_2 ; P – GaP; Ca – wollastonite; Ti – titanium; Fe – iron; Br – KBr. A Everhart-Thornley type (YAG Crystal) secondary electron detector was used with a 20 kV accelerating voltage. First, the samples were mounted on a sample holder with double-sided adhesive conductive carbon tape. The minerals were analyzed in high vacuum mode (pressure of 0.018 Pa). The samples were introduced into large analytical chamber equipped with a fully motorized five-axis stage (x - y - z , rotation, and tilt). VegaTC control software on the Windows™ operating system was used for data collection.

The XRPD measurements were performed using an XRD-6100 Diffractometer (Shimadzu, Japan). CuK_α radiation (1.54178 Å, nickel K_β filter was used) was applied, and current and tube voltage regimes of 30 mA and 40 kV were set, respectively. The samples were powdered and scanned over a constant detector rotation speed of 1.2°/min in increments of 0.02° within the 10–70° 2θ range. The most intense maxima in the diffraction patterns were compared with the corresponding patterns from the PDF-2 database (Gates-Rector & Blanton, 2019).

Micro-Raman spectra were acquired in the spectral range from 100 to 2000 cm^{-1} on a LabRam 300 Infinity micro-Raman multichannel spectrometer (Horiba JobinYvon, Japan) using the 632.81 nm internal He:Ne laser. The backscattered radiation (180° configuration) was analyzed with an 1800

lines/mm grating monochromator. Raman intensities were collected with a thermo-electrically cooled CCD array detector. An Olympus MPlanN confocal microscope equipped with the Olympus LMPlanFL $\times 50$ long-distance objective (N.A=0.5) with a working distance of 10.6 mm was used. In order to focus the laser beam, the position on the sample surface was adjusted using a motorized x-y stage. A 500 μm pinhole and 100 μm slit were selected. No attenuation filter was used, and the laser power of 4.21 mW on the samples was measured by a LaserCheck™ Handheld Power Meter (Coherent Scientific, Australia). The acquisition time for spectral collection, depending on the sample and its fluorescence, varied from 5 to 20 seconds, whereas the number of accumulations also was adjusted from 5 to 20. The Rayleigh line and the 520.5 cm^{-1} band of a Si standard were used during the calibration.

In order to obtain the spectral information from the glassy samples, a baseline correction (Labspec software) aid to distinguish two spectral regions for the Si–O stretching and Si–O bending vibrations observed around 1,100–1,000 cm^{-1} and 550–500 cm^{-1} , respectively. This operation enables one to retain only the molecular Si–O Raman signature, valuable for determination of the intensity ratio of the A_{500}/A_{1000} bands, the so called polymerization index, I_p (Colomban, 2003). The obtained spectra were curve fit using Gaussian profiles (Colomban, Tournié, et al., 2006).

RESULTS AND DISCUSSION

The compositional and structural features of the samples by means of XRPD and SEM-EDS.

X-ray powder diffraction methods have been more extensively used in the last 20 years in the characterization of different crystalline and non-crystalline materials of archaeological, historic, and cultural interest (e.g. Antonelli & Nestola, 2021; Franceschi, 2014; Garrison, 2014; Moon et al., 2021; Nakai & Abe, 2012; Schreiner et al., 2004). On the other hand, advances in automated scanning electron microscopy combined with energy dispersive spectrometers (SEM-EDS) have created the potential to offer a seamless combination of textural and mineralogical data based on the acquisition of energy dispersive spectra that has so far been unattainable with other existing techniques (e.g., Conventi et al., 2012; Knappett et al., 2011; Kuisma-Kursula, 2000; Valderrama et al., 2019). Both approaches were used here and provide a complementary profile for both the chemical and mineralogical features of the analyzed samples.

The XRPD patterns for all 12 samples are presented in Figure S3. All observed maxima are assigned to corresponding minerals in comparison to the literature (Table 1). From the results it can be inferred that some of the samples (3, 4, 5) are totally amorphous, whereas Samples 8 and 9 are predominantly amorphous but also contain crystalline phases (Table 1, Figure S3). The remaining samples (1, 2, 6, 7, 10, 11, and 12) are entirely crystalline indicating the presence of the minerals quartz (SiO_2), magnesite (MgCO_3), hematite (Fe_2O_3), ankerite [$\text{Ca}(\text{Fe}^{2+}, \text{Mg}, \text{Mn}^{2+})(\text{CO}_3)_2$], dolomite [$\text{CaMg}(\text{CO}_3)_2$], wüstite (FeO), and cuprite (Cu_2O).

The XRD pattern of Sample 1 (Figure S3, a) showed only a single phase, revealing the characteristic peaks for magnesite, MgCO_3 (Anthony et al., 1990) (Table 1). The chemical composition of the sample determined by EDS analysis has confirmed only the presence of MgO and CO_2 corresponding to the magnesite composition (Table 2, Figure 2).

The XRPD pattern of Sample 2 (Figure S3, b) showed three minerals, quartz, dolomite, $\text{CaMg}(\text{CO}_3)_2$, and magnesite (Table 1). These results have proved the crystalline nature of SiO_2 in this stone. The presence of quartz and magnesite was also determined by SEM-EDS (Figure 2, Table 2).

On the other hand, the XRPD patterns of Sample 3 (Figure S3, c) exhibit an amorphous and vitreous character of corresponding well to the glassy features in the SEM micrograph (Figure 2, sample 3). Similarly, the X-ray powder diagrams of Samples 4 and 5 (Figure S3, d and e) indicate amorphous-vitreous nature of the samples, evident from the wide halo peak in the 12.5–35° region for 2θ , attributed to the amorphous silica content. In addition, on this broad hump, two wide peaks centered at 14.2–14.3 and at 16.7–16.9° 2θ can be seen for samples 4 and 5. Such peaks are typical

TABLE 1 The registered maxima in the XRD diagrams of the analyzed samples compared and assigned to the presence of the minerals (M – magnesite; Q – quartz, D – dolomite, A – ankerite, C – cuprite, W – wüstite)

Sam. No	1	2	3	4	5	6
Peaks (2 θ and-value)	32.35;2.76 (32.56;2.74-M)	20.66;4.29 (20.84;4.25-Q)	12.65–36.0; 7.00–2.50 (halo)	12.65–36.0; 7.00–2.50 (halo)	12.65–36.0; 7.00–2.50 (halo)	20.63;4.30 (20.63;4.29-Q)
	35.54;2.52 (35.74;2.5-M)	24.89;3.57 (25.07;3.54-M)				22.10;4.01 (21.92;4.05-A)
	38.55;2.33 (38.74;2.32-M)	26.45;3.36 (26.65;3.34-Q)				23.76;3.74 (23.93;3.71-A)
	42.69;2.11 (42.86;2.10-M)	30.73;2.90 (30.81;2.89-D)				26.38;3.37 (26.42;3.36-Q)
	46.54;1.94 (46.73;1.94-M)	32.34;2.76 (32.56;2.74-M)				30.59;2.92 (30.74;2.90-A) (30.81;2.89-D)
	51.34;1.77 (51.62;1.76-M)	35.51;2.52 (35.74;2.51-M)				33.10;2.70 (33.24;2.69-A) (33.34;2.68-D)
	53.56;1.70 (53.71;1.70-M)	36.35;2.46 (36.54;2.45-Q)				36.32;2.47 (36.15;2.48-Q)
	61.07;1.51 (61.29;1.51-M)	38.58;2.33 (38.74;2.32-M)				37.01;2.42 (37.21;2.41-A)
	62.11;1.49 (62.25;1.49-M)	39.27;2.29 (39.45;2.28-Q)				39.27;2.29 (39.24;2.29-Q)
	66.11;1.41 (66.22;1.41-M)	40.93;2.20 (41.00–2.19-D)				40.76;2.21 (40.93;2.20-A)
	69.10;1.36 (69.17;1.35-M)	42.27;2.13 (42.46;2.12-Q)				42.15;2.14 (41.98;2.14-Q)
		42.70;2.11 (42.86;2.10-M)				44.56;2.03 (44.73;2.02-A)
		45.61;1.98 (45.80;1.97-Q)				49.92;1.82 (49.75;1.83-Q) (49.04;1.85-A)
		46.58;1.94 (46.73;1.94-M)				50.60;1.80 (50.43;1.80-Q) 50.13;1.81-A)
		49.96;1.82 (50.13;1.81-Q)				54.66;1.67 (54.41;1.68-Q)
		50.87;1.79 (50.91;1.79-D)				59.54;1.55 (59.58;1.55-A) (59.68;1.54-D)
		51.34;1.77 (52.77;1.73-M)				65.58;1.42 (65.07;1.42-A)
		53.49;1.71 (53.71;1.70-M)				67.08;1.39 (67.09;1.39-A) (67.25;1.39-D)
		54.70;1.67 (54.86;1.67-Q)				67.80;1.38 (67.65;1.38-Q) (67.55;1.38-A) (67.25;1.39 D)
		59.78;1.54 (59.68;1.54-D) 59.94;1.54-Q)				
		61.08;1.51 (61.29;1.51-M)				
		62.11;1.49 (62.25;1.49-M)				
		66.12;1.41 (67.25;1.39-D) (66.27;1.40-M)				
		67.60;1.38 (67.74;1.38-Q)				
		68.03;1.37 (68.12;1.37-Q)				
		69.00;1.35 (69.17;1.35-M)				
ICDD entries	Magnesite 0 0360383	Magnesite 0 0360383 Quartz 0 0331161 Dolomite 0 0340517				Quartz 0 0741811 Dolomite 0 0340517 Ankerite 0 0410586

TABLE 1 (Continued)

Sam. No	7	8	9	10	11	12
Peaks (2theta-d-value)	32.43;2.75 (32.63;2.74-M)	12.65–36.0; 7.00–2.50 (bale)	36.05;2.48 (36.19;2.48-W)	20.67;4.29 (20.63;4.29-Q)	20.70;4.28 (20.85;4.25-Q)	20.50;4.33 (20.63;4.29-Q)
	35.63;2.51 (35.84;2.50-M)	32.40;2.76 (32.63;2.74-M)	36.83;2.44 (36.80;2.44-C)	26.50;3.36 (26.42;3.36-Q)	26.47;3.36 (26.63;3.34-Q)	26.25;3.35 (26.42;3.36-Q)
	38.64;2.32 (38.81;2.31-M)		41.94;2.15 (41.98;2.15-W)	30.69;2.91 (30.81;2.89-D)	32.99;2.71 (33.15;2.70-H)	36.16;2.48 (36.15;2.48-Q)
	42.79;2.11 (42.99;2.10-M)		42.90;2.12 (42.61;2.12-C)	33.04;2.70 (33.34;2.68-D)	35.45;2.52 (35.61;2.51-H)	39.05;2.30 (39.24;2.29-Q)
	46.63;1.94 (46.81;1.93-M)		60.61;1.52 (60.89;1.52-W)	36.48;2.46 (36.15;2.48-Q)	36.37;2.46 (36.54;2.45-Q)	40.05;2.25 (40.29;2.23-Q)
	51.40;1.77 (51.62;1.76-M)		61.69;1.50 (61.79;1.50-C)	39.35;2.28 (39.24;2.29-Q)	39.28;2.29 (39.24;2.29-Q)	42.04;2.14 (41.98;2.14-Q)
	53.65;1.70 (53.88;1.70-M)			40.76;2.21 (41.00;2.19-D)	40.10;2.24 (40.29;2.23-Q)	45.32;1.99 (45.33;1.98-Q)
	61.19;1.51 (61.34;1.51-M)			42.32;2.13 (42.44;2.12-Q)	42.26;2.13 (42.44;2.12-Q)	49.74;1.83 (49.75;1.83-Q)
	62.20;1.49 (62.35;1.48-M)			49.99;1.82 (49.75;1.83-Q)	45.61;1.98 (45.79;1.97-Q)	59.54;1.55 (59.31;1.55-Q)
	66.20;1.41 (66.43;1.40-M)			59.78;1.54 (59.68;1.54-D) (59.31;1.55-Q)	49.31;1.84 (49.47;1.84-H)	63.70;1.46 (63.61;1.46-Q)
	69.11;1.35 (69.34;1.35-M)			67.46;1.38 (67.25;1.39-D) (67.85;1.38-Q)	49.95;1.82 (50.13;1.81-Q)	67.36;1.38 (67.54;1.38-Q)
					53.91;1.69 (54.08;1.69-H)	
					59.77;1.54 (59.95;1.54-Q)	
					63.81;1.45 (63.98;1.45-H)	
					67.59;1.38 (67.74;1.38-Q)	
					68.00;1.37 (68.14;1.37-Q)	
ICDD entries	Magnesite 0 0080479	Magnesite 0 0080479	Wustite 0 0021180 Cuprite 0 0030898	Quartz 0 0010649 Dolomite 0 0340517	Quartz 0 0461045 Hematite 0 0330664	Quartz 0 0741811

TABLE 2 Chemical composition of the analyzed samples by EDS (in wt.%)

Element	SiO ₂	Al ₂ O ₃	CaO	MgO	FeO	K ₂ O	Na ₂ O	CuO	PbO	SO ₂	Cl	CO ₂	Total
Sample number	1	-	-	-	39.10	-	-	-	-	-	-	60.09	100.00
	2	1.50	-	-	31.84	3.61	-	-	-	-	-	63.05	100.00
	3	73.48	6.67	4.51	1.69	2.37	6.46	-	-	4.82	-	-	100.00
	4	62.70	2.29	4.40	-	-	0.85	28.03	-	-	1.73	-	100.00
	5	47.81	-	2.68	-	-	-	36.50	-	13.01	-	-	100.00
	6	20.66	-	26.13	9.11	2.45	1.22	-	-	-	-	40.43	100.00
	7	1.52	-	3.78	40.08	-	-	-	-	-	-	54.62	100.00
	8	53.51	5.55	8.31	12.46	2.29	2.51	5.49	-	9.89	-	-	100.00
	9	51.00	2.65	9.69	2.58	3.22	1.78	16.88	9.56	2.64	-	-	100.00
	10	2.71	-	1.18	30.83	-	-	-	-	-	-	65.28	100.00
	11	96.91	-	-	-	3.09	-	-	-	-	-	-	100.00
	12	100.00	-	-	-	-	-	-	-	-	-	-	100.00

for the sodium silicate glasses (Abdel Wahab et al., 2020). The presence of Na (in addition to Si) in the glassy Samples 3 and 4 was confirmed by the EDS results (Table 2, Figure 2). EDS also indicated the near-complete absence of MgO and K₂O (only small fraction of K₂O was determined in Sample 4). Based on these EDS results, it could be postulated that natron was added as flux (Freestone, 1994) in Samples 4 and 5. That postulate agrees with the results considering that the Na-rich glass contains more than 12 wt% of Na₂O and less than 5 wt% of K₂O. On the other hand, the detection of Pb suggests that it was added to the glass to achieve desired characteristics, that is, its opacity and color. Many of the colorants added to ancient soda lime-silica glass contained lead, in particular those for opaque red and yellow, and for green made from a mixture of yellow and blue colorants. Thus, although the content of PbO determined in Sample 5 is especially high (13.1 wt%), its quantity is low compared to the 20 wt.% found in some glass mosaic tesserae from Pompeii (Arletti et al., 2006). No carbonates were determined in samples 3–5, revealing their nominally silicate character (Table 2).

Samples 3–5 (Figure 2c–e) had a more specular and translucent appearance compared to the other specimens whose surfaces were more opaque and less reflective. Such appearance is characteristic of silicate glasses that, containing no dispersed crystalline domains or grain boundaries, tend to exhibit specular surface reflection rather than diffuse subsurface scattering. Another distinct morphological characteristic of glassy Samples 3–5 were circular features with diameters of up to 10 μm in Samples 3 and 5, and up to 50 μm in Sample 4. Such features were a strong indicator of the existence of fluid inclusions trapped in the matrix (Figure 2c–e, arrow marks). Furthermore, the glassy character of the samples was confirmed through their Raman spectral signatures.

The XRPD pattern of Sample 6 (Figure S3, f) revealed characteristic peaks for the following minerals: quartz, ankerite [Ca (Fe,Mg)(CO₃)₂], and dolomite (Table 1). The presence of these crystalline phases were also deduced from the SEM-EDS results (Table 2, Figure 2), with the ankerite occurring as anhedral to subhedral crystals in the matrix (Goldsmith et al., 1962; Rosenberg, 1991).

The XRPD pattern of sample 7 (Figure S3, g) demonstrated a mineral phase typical for magnesite with 11 diffraction peaks matching the values reported in the literature (Table 1). The chemical composition determined by EDS, showed that magnesite is the dominant phase, but 3.78 wt.% of CaO was also present (Table 2) possibly indicating the co-association of dolomite, CaMg (CO₃)₂ (not detected by XRD), with magnesite, MgCO₃.

The XRPD patterns of Samples 8 and 9 (Figure S3, h and i) indicate that the material is predominantly amorphous/vitreous. However, the appearance of narrow peaks establish the presence of some crystalline material. In Sample 8, besides the amorphous phase, the strongest peak of magnesite, corresponding to a *d*-spacing of 2.75 Å (32.40°), can be seen, whereas the multiple peaks of Sample 9

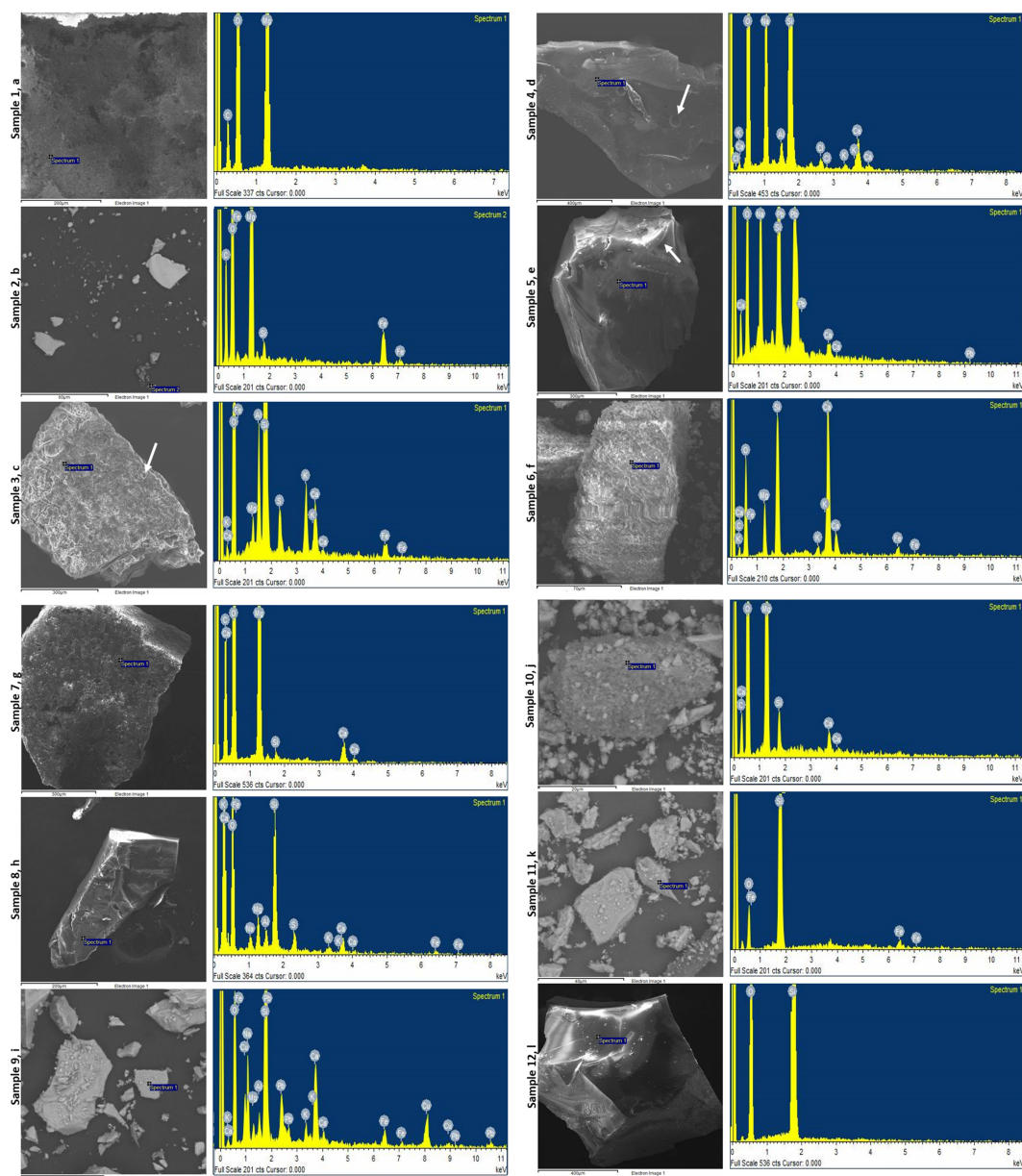


FIGURE 2 SEM/EDS of samples denoted 1–6 (a–f) (A panel) and 7–12 (g–l) (B panel) [Color figure can be viewed at wileyonlinelibrary.com]

indicate the presence of iron- and copper-containing minerals: wüstite, FeO (2.48 \AA at 36.05° ; 2.15 \AA at 41.94° and 1.52 \AA at 60.61°), and cuprite, Cu_2O (2.44 \AA at 36.83° , 2.12 \AA at 42.90° and 1.50 \AA at 61.69°) (Table 1) (Gates-Rector & Blanton, 2019). Wüstite is widespread in the soluble fraction of soils and weathered rock (Chandy, 1965), whereas cuprite appears as a secondary mineral formed by the weathering of copper sulfide minerals (Veblen & Post, 1983).

The XRPD pattern of sample 10 (Figure S3, j) revealed characteristic peaks for the following minerals: quartz and dolomite (Table 1) (Gates-Rector & Blanton, 2019). The rather high content of carbon (expressed as CO_2 in Table 2) determined by EDS originates from both the charred wooden

remains and from the dolomite phase. The SEM micrographs indicated surface variations, attributed to the different temperature conditions during the fire. The fire likely also deposited some pyrolytic carbon on samples 1, 2, 6, 7, 10, and 12.

The XRPD pattern of Sample 11 (Figure S3, k) that was assembled as triangular pieces in the restored sectile panel (and surround the square pieces designated as Sample 12, Figure 1) contained the characteristic peaks for quartz, but also exhibited characteristic peaks for hematite (Table 1). The latter mineral contributes to the color of the sample. The red color of hematite is not vivid and intense but closer to brown, as evident from the sample's appearance. However, the complementary EDS analysis indicated the presence of iron, in addition to the dominant SiO₂ signal (Table 2), and confirmed that the sample is composed of only hematite and crystalline quartz.

The most impressive and transparent pieces of the sectile panel were numbered Sample 12 (Figure 1). According to the XRPD pattern (Figure S3, l), those samples consist of pure quartz, having the following characteristic peaks: 4.33 Å at 20.50°; 3.35 Å at 26.25°; 2.48 Å at 36.16°; 2.30 Å at 39.05°; 2.25 Å at 40.05°; 2.14 Å at 42.04°; 1.99 Å at 45.32°; 1.83 Å at 49.74°; 1.55 Å at 59.54°; 1.46 Å at 63.70°; 1.38 Å at 67.36°) (Table 1). No other mineral was identified in the EDS analysis showing that these nice rhombus-shaped pieces from the sectile panel were cut from rock crystal (Figure 1).

Raman spectra and identification of minerals and glasses

A number of papers identify Raman spectroscopy as one of the most powerful and general instrumental techniques for identifying and characterizing compounds (minerals) present in objects of archeological, historical, and artistic importance (e.g., Casadio et al., 2016; Colomban, 2003, 2004, 2005; Colomban et al., 2020; Colomban, Etcheverry, et al., 2006; Colomban, Tournié, et al., 2006; Galli et al., 2004; Guo et al., 2020; Madariaga & Candeias, 2019; McMillan, 1989; Nasdala & Schmidt, 2020; Reiche et al., 2004). Raman spectroscopy is particularly useful in the study of the ancient ceramics and glasses. In addition to the contribution from other prominent researchers in this field (e.g. Casadio et al., 2016; Edwards & Chalmers, 2005; Galli et al., 2004; Henderson, 2013; Robinet et al., 2008), much foundational work on the study of glassy phases for the archeological purposes have been obtained and published by Colomban and coworkers. Namely, they have proposed a tentative guide to identify different types of glassy silicates and to classify them as a function of their composition (Colomban, 2004; Colomban, Tournié, et al., 2006). Their classification scheme includes seven families of glassy silicates differentiated by peak area ratios (A_{500}/A_{1000} - named the polymerization index, I_p) of the Si–O bending band (around 500 cm⁻¹) and stretching band (around 1,000 cm⁻¹), and the different components of the latter peak (see Figures 4 and 9 in Colomban, Tournié, et al., 2006 and the references therein). Direct relationships between the silica content (more precisely, the ratio between the glass-former, mainly Si and Al oxides) and the flux content (Na, K, Ca, Pb oxides) and the properties of glassy silicate have been established. They have also demonstrated the validity of the classification scheme by correlating the compositional parameters with the melting/processing temperature of the seven glass families (see Figure 7 in the paper by Colomban, Tournié, et al., 2006).

The Raman spectrum of Sample 1 (Figure 3a), although exhibiting strong fluorescence, indicates rather pronounced similarity with the corresponding spectrum of magnesite (Figure 3b) (Krishnamurti, 1956; Rutt & Nicola, 1974), corroborating the XRPD results. Normal mode analysis in magnesite revealed two external Raman active modes (librational, E_g , and translational, E_g) as well as three internal (one A_{1g} , and two E_g) Raman active modes (Rutt & Nicola, 1974). The peaks in the Raman spectrum attributed to the external modes were observed at 329 and 212 cm⁻¹ whereas the internal modes were observed at 1092 cm⁻¹ (A_{1g}) and 734 cm⁻¹ (E_g).

The Raman spectrum of sample 2 (Figure 3c) exhibits very distinct bands at 1093, 324, 209, and one weak maximum at 737 cm⁻¹ that are typical for magnesite mineral (Spivak et al., 2014). The strongest band at 1093 cm⁻¹ (A_{1g}) is attributed to the symmetric stretching carbonate vibration

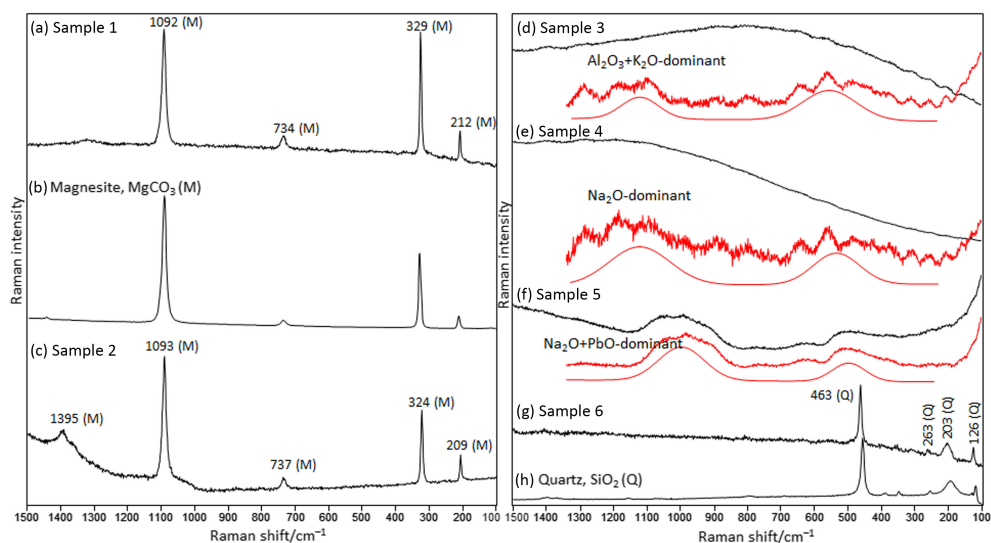


FIGURE 3 Raman spectra of Samples 1 to 6 *Notes:* The spectrum of pure magnesite (b) and quartz (h) are presented for comparison and to address the corresponding bands (given by an appropriate acronym) that appear in the spectra of the analyzed samples. The spectra of the glassy samples 3–5 were baseline corrected (noisy red line) and subsequently curve fitted (smooth black line) to extract the information for Si–O stretching (1,000–1,100 cm^{-1}) and Si–O bending (550–500 cm^{-1}) bands from the “ SiO_4 ” molecular units. The following instrumental conditions for acquisition time (AT) and accumulation number (AN) were carefully adjusted to obtain good signal-to-noise ratio for each spectrum: Sample 1 (AT = 15 s, AN = 15), Sample 2 (AT = 5 s, AN = 6), sample 3 (AT = 15 s, AN = 15), Sample 4 (AT = 15 s, AN = 15), Sample 5 (AT = 15 s, AN = 15), Sample 6 (AT = 15 s, AN = 15). [Color figure can be viewed at wileyonlinelibrary.com]

$[\nu_1(\text{CO}_3)]$, whereas the band at 737 cm^{-1} (E_g) is attributed to the in-plane bending mode $[\nu_4(\text{CO}_3)]$. The lower frequency bands at 209 and 329 cm^{-1} appear from the translational (E_g) and librational (E_g) external mode, respectively (Boulard et al., 2012). However, the spectrum reveals one wide and weak intensity band at 1395 cm^{-1} that is attributed to the antisymmetric stretching carbonate vibration $[\nu_3(\text{CO}_3)]$, which occasionally appears in the Raman spectra of carbonate minerals around $1,400 \text{ cm}^{-1}$ (Frost et al., 2008; Ma et al., 2021). The presence of carbonate was confirmed by the XRPD and SEM-EDS results.

The raw Raman spectra of the Samples 3, 4, 5 (Figure 3d–f) showed no sharp bands, due to their amorphous and glassy nature. The discussion of the Raman spectra of these glasses was rendered in accordance with the valuable findings presented by Colomban, Tournié, et al., 2006. The raw spectra were pre-processed and the baselines were subtracted in order to only keep the “ SiO_4 ” molecular signature that is essential to recognize the type of the glassy silicate (Figure 3d–f). It was found that the glassy properties changed in accordance with the variation of the flux elements, as determined by EDS analysis (Table 2). The glassy polymerization index (A_{500}/A_{1000}) was found to be highest ($I_p = 1.91$) in Sample 3 where the dominant flux elements were Al, K, and Ca (expressed as oxides, from 6.67 to 4.51 wt%, Table 2). These results are in agreement with the literature (Colomban, 2003; Colomban, Tournié, et al., 2006), where the highest I_p is found for $\text{K}_2\text{O} + \text{CaO} + \text{Al}_2\text{O}_3$ -containing glassy silicates. In contrast, the I_p for glassy Samples 4 and 5 was significantly lower (0.62 and 0.40, respectively) corroborating the conclusions that Na_2O -dominant glasses (28.03 and 36.5 wt%, respectively) exhibit values of I_p below 1. The somewhat lower I_p of Sample 5 (0.40) is attributed to the additional presence of PbO (13.01 wt%). Upon classifying this sample as $\text{Na}_2\text{O} + \text{PbO}$ glass, the index fits in the 0.4–0.5 I_p range found for these type of glasses (Colomban, Tournié, et al., 2006). Aside from the effect of PbO on the I_p , the Raman spectra of the Glass 5 exhibited a redshift of the ν_{max} (Si–O) Raman band to around $1,000 \text{ cm}^{-1}$ (Figure 3f), falling in the range between PbO-rich (960 – 980 cm^{-1}) and PbO + Na_2O -bearing ($1,020$ – $1,050 \text{ cm}^{-1}$) glasses (Colomban, Tournié, et al., 2006). The absence of Pb

in Samples 3 and 4 is reflected in the position of the band centroid around $1,100\text{ cm}^{-1}$ (Figure 3d-e), typical for $\text{Na}_2\text{O}+\text{K}_2\text{O}+\text{CaO}$ and $\text{K}_2\text{O}+\text{CaO}$ glasses (Colomban, Tournié, et al., 2006). The results also confirmed that the lower A_{500}/A_{1000} values corresponded to silica-poor compositions (Colomban, 2003) for Glasses 4 and 5 (Table 2).

The empirical relationship between I_p , the glass composition and the processing temperature is well documented (Colomban, 2003; Colomban, Tournié, et al., 2006) and has also been adopted by different groups (Ollier et al., 2004; Prinsloo et al., 2005). It was used to estimate the firing temperature of the analyzed glasses (Samples 3–5). According to this classification, the first family ($I_p < 0.3\text{--}0.5$) mostly corresponds to lead-rich silicates processed at low temperatures ($<700^\circ\text{C}$) and is also the case for Sample 5 ($I_p = 0.40$). Sample 4 fits in the second family ($0.5 < I_p < 0.8$) of silicates processed at medium temperature (800°C). According to this parameter, Sample 3 ($I_p = 1.91$), corresponds to the Ca-based glassy family ($1.3 < I_p < 2.5$) and although it contains significant K-content giving $2.5 < I_p$, its processing temperature could be estimated to be above $1,100^\circ\text{C}$ ($1,000^\circ\text{C}$ for $I_p \sim 1$ and $\sim 1,400^\circ\text{C}$ for $I_p \sim 7$, Colomban, 2003).

The Raman spectrum of Sample 6 shows the characteristic peaks of the dominant mineral, quartz, though the other phases, which were determined by XRD (ankerite and dolomite), could not be seen in the Raman spectrum. Obviously, their presence is diminished by the strong Raman susceptibility of quartz.

Sample 7 comprised a black coating over a white core material. Sample 8 was taken from a similar piece but had the appearance of charred wood. On the higher wavenumber part of the Raman spectrum (Figure 4a) collected from the averaged Sample 7, typical bands for the presence of carbon black (Figure 4b) evolved (Jawhari et al., 1995; Pawlyta et al., 2015). Namely, the very broad band centered at 1340 cm^{-1} and the somewhat sharper band centered at 1596 cm^{-1} are attributed to graphite bands, known as D and G bands, respectively. The G band is assigned to the in-phase vibration of the graphite lattice whereas the D band is a disorder band caused by the graphene edges (Tuinstra & Koenig, 1970). A universal observation is that these bands are broader in highly disordered graphite,

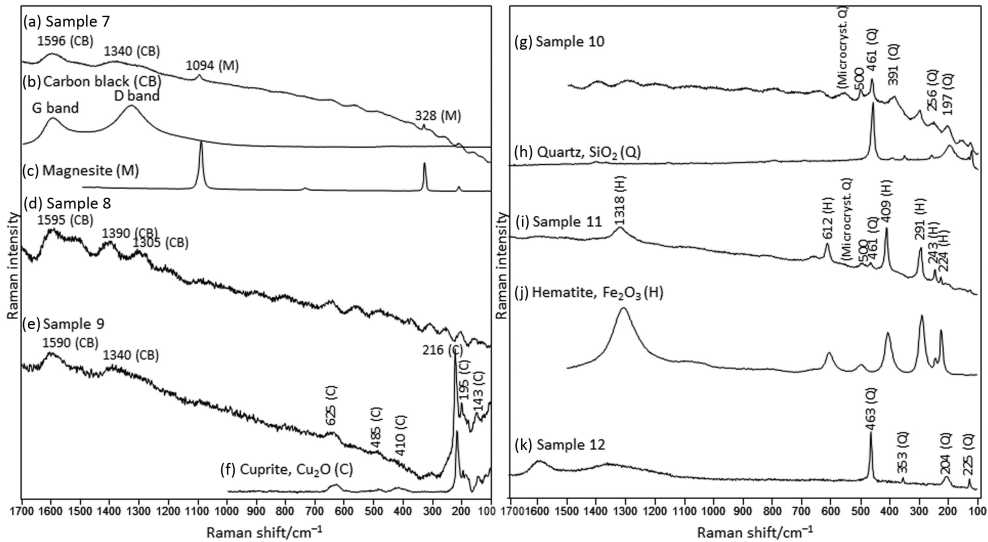


FIGURE 4 Raman spectra of Samples 7 to 12 Notes: The spectra of pure carbon black (b), magnesite (c), cuprite (e), quartz (g) and hematite (i) are presented for comparison and to address the corresponding bands (given by an appropriate acronym) that appear in the spectra of the analyzed samples. The following instrumental conditions for acquisition time (AT) and accumulation number (AN) were carefully adjusted to obtain good signal-to-noise ratio for each spectrum: Sample 7 (AT= 10 s, AN=10), Sample 8 (AT= 8 s, AN=8), Sample 9 (AT= 20 s, AN=20), Sample 10 (AT= 12 s, AN= 12), Sample 11 (AT= 5 s, AN= 5), Sample 12 (AT= 5 s, AN= 5).

with the D band exhibiting higher relative intensity compared to the G band (Kudin et al., 2008), as was here observed (Figure 4a). From these results, one can infer that the amorphization of graphite is very pronounced suggesting incomplete combustion of organic material such as wood resulting in the deposition of carbon black over the analyzed specimen. The lower part of the spectrum (Figure 4a) has shown the two strongest magnesite (Figure 4c) Raman bands at 1094 and 328 cm^{-1} , confirming its presence in the core, inner part of the sample that was also identified by XRPD (see previous discussion, Table 1 and Figure S3, g). On the other hand, the Raman spectrum of Sample 8 (Figure 4d) shows less defined features in the Raman spectrum of graphite pointing to more severe fire damage in that area of the mosaic.

Sample 9 had a very inhomogeneous surface texture seen by the presence of black spots and ochre-yellow fragments. The Raman spectrum (Figure 4e) illustrates a two component mixture. First, D and G bands of the carbon black (1,590 and 1,340 cm^{-1}) can be seen. The carbon peaks are accompanied by prominent peaks at lower wavenumbers: 625, 485, 410, 216 (strongest), 195 and 143 cm^{-1} coinciding with the Raman bands from cuprite, Cu_2O (Figure 4f) (Ciupiński et al., 2010). This result explains that initial corrosion that took place in the contact region with the copper, appearing as the patina layer. The assignment of the bands from the carbon black in this sample (Figure 4e) confirmed its presence as an external contaminant (from the fire that occurred in the building).

The Raman spectra of Samples 10 and 11 (Figure 4g and i) exhibit the most prominent band for quartz at 461 cm^{-1} (Figure 4h), whereas in Sample 10, weaker bands at 391, 256 and 197 cm^{-1} can also be made out (Figure 4g) (Krishnan, 1945) indicating the presence of this mineral. Here, it should be emphasized that the Raman band at 500 cm^{-1} , also present in the spectra of Samples 10 and 11, is distinctive fingerprint of microcrystalline quartz inclusions (chalcedony, moganite) (Heaney et al., 2007; Miriello et al., 2015) (Figure 4g,i). However, Sample 11 also exhibited stronger bands (Figure 4h) as at 1318 (2LO), 612 (E_g), 409 (E_g), 291 (E_g), 243 (E_g), and 224 (A_{1g}) cm^{-1} from the dominant phase, hematite (Figure 4j) (Mäkie et al., 2011; Marshall & Olcott Marshall, 2011). The 1,318 cm^{-1} peak, occurs very close to the frequency of the carbon D band (A_{1g} mode at 1340 cm^{-1}), and one should be careful to precisely ascribe this band to hematite and not to the mixture of carbonaceous material with hematite. Here, this peak originates solely from the 2LO hematite mode resulting from the defects in the hematite lattice. No presence of organic carbon has been evidenced lacking the maxima at 1340 cm^{-1} .

The bands in the spectrum of Sample 12, occurring at 463, 353, 204 and 125 cm^{-1} (Figure 4k), demonstrated the crystalline quartz origin of the specimen, whereas the two wide and weak bands above 1,000 cm^{-1} confirmed the presence of char on the surface as a result of the fire. The adjacent position of the black wooden sticks to the transparent pieces (Sample 12 was one of them) as seen in the mosaic (Figure S2, Supplementary Material) justifies the negligible presence of char on the surface of Sample 12.

CONCLUSIONS AND FUTURE PROSPECTS

It was confirmed that the complementary use of XRPD, SEM-EDS and Raman spectroscopy gives useful mineralogical and chemical findings mainly with a nondestructive approach. Their combined use has shown that the colorful opus sectile panel discovered at the Episcopal Residence in the ancient city of Stobi (fourth–sixth century AD) consisted of seven different mineral samples (magnesite, quartz, dolomite, ankerite, cuprite, wüstite, and hematite). The use of the so called glassy polymerization index, I_p , has revealed that three of these samples belong to $\text{Al}_2\text{O}_3 + \text{K}_2\text{O}$ -dominant, Na_2O -dominant, and $\text{Na}_2\text{O} + \text{PbO}$ -dominant glassy silicate type.

The obtained results by various experimental techniques are comparable and mainly correspond to each other. The rarely observed differences are principally due to the presence of low amount of mineral components in the studied samples being not equally recognizable by used techniques.

Some of the determined minerals could be connected to Macedonian geology (dolomite, hematite, and magnesite). The remaining minerals (ankerite, wüstite, cuprite), the glassy samples as well as the fully transparent quartz varieties are not typical for Macedonian territory. The latter circumstance supports the archaeological assumption that the panel was brought from a distant and early Christian population center. Such conclusion is based on the artistic characteristics and religious symbolism of the panel, as well as on the fact that during the one century ongoing excavations, similar findings has neither been found in Stobi nor in the neighboring Balkan countries.

The obtained results in this study could be taken as a relevant basis for further comparative studies aimed at determining the exact origin of the discovered panel would provide a general historical interpretation of the cultural and other relations of Stobi with the surrounding early Christian world.

ACKNOWLEDGEMENTS

Three anonymous reviewers who contributed to improve the quality of the work are acknowledged. The proofreading undertaken by Professor Joseph Graham from Missouri University of Science and Technology, USA, is appreciated. The handling of peer review of the manuscript by Managing Editor Dr. Ina Reiche is also thanked.

CONFLICTS OF INTEREST

The authors declare no conflict of interest.

PEER REVIEW

The peer review history for this article is available at <https://publons.com/publon/10.1111/arc.12834>.

DATA AVAILABILITY STATEMENT

All supporting data can be found in the online supplementary files with this paper.

ORCID

Petre Makreski  <https://orcid.org/0000-0003-0662-5995>

Arianit A. Reka  <https://orcid.org/0000-0002-6419-2270>

REFERENCES

- Abdel Wahab, E. A., Shaaban, K. S., & Yousef, E. S. (2020). Enhancement of optical and mechanical properties of sodium silicate glasses using zirconia. *Optical and Quantum Electronics*, 52, 458. <https://doi.org/10.1007/s11082-020-02575-3>
- Aleksova, B. (1985). The old episcopal basilica at Stobi. *Annual Proceedings of the Faculty of Philosophy*, Skopje, 38. (in Macedonian).
- Aleksova, B. (1997). *Loca sanctorum Macedoniae: the cult of martyrs in Macedonia from the 4th to the 9th centuries*. Makedonska Civilizacija.
- Anthony, J. W., Bideaux, R. A., Bladh, K. W., & Nichols, M. C. (1990). *Handbook of mineralogy*. Mineral Data Publishing.
- Antonelli, F., & Nestola, F. (2021). An innovative approach for provenancing ancient white marbles: the contribution of x-ray diffraction to disentangling the origins of Göktepe and Carrara marbles. *Scientific Reports*, 11, 22312. <https://doi.org/10.1038/s41598-021-01800-7>
- Arletti, R., Quartieri, S., & Vezzalini, G. (2006). Glass mosaic tesserae from Pompeii: an archeometrical investigation. *Periodico di Mineralogia*, 75, 25–38.
- Beran, A., & Libowitzky, E. (Eds.). (2004). *Spectroscopic methods in mineralogy (EMU notes in mineralogy)* (Vol. 6). Mineralogical Society of Great Britain and Ireland. <https://doi.org/10.1180/EMU-notes.6>
- Boev, B., Šijakova-Ivanova, T., Robeva-Čukovska, L., & Boev, I. (2008). Mineral researches of the examples of the archeological locality “Stobi” using the method of the X-ray diffraction. *Geologica Macedonica*, 22, 27–41.
- Boulard, E., Guyot, F., & Fiquet, G. (2012). The influence on Fe content on Raman spectra and unit cell parameters of magnesite–siderite solid solutions. *Physics and Chemistry of Minerals*, 39, 239–246. <https://doi.org/10.1007/s00269-011-0479-3>
- Casadio, F., Céline Daher, C., & Bellot-Gurlet, L. (2016). Raman spectroscopy of cultural heritage materials: overview of applications and new frontiers in instrumentation, sampling modalities, and data processing. *Topics in Current Chemistry*, 374, 62. <https://doi.org/10.1007/s41061-016-0061-z>
- Chandy, K. C. (1965). An occurrence of wüstite. *Mineralogical Magazine*, 35, 664–666. <https://doi.org/10.1180/minmag.1965.035.272.13>

- Chen, L., Xu, J., & Chen, J. (2015). Applications of scanning electron microscopy in earth sciences. *Science China Earth Sciences*, 58, 1768–1778. <https://doi.org/10.1007/s11430-015-5172-9>
- Choudhary, O. P., & Choudhary, P. (2017). Scanning electron microscope: Advantages and disadvantages in imaging components. *International Journal of Current Microbiology and Applied Sciences*, 6, 1877–1882. <https://doi.org/10.20546/ijemas.2017.605.207>
- Ciliberto, E., & Spoto, G. (Eds.). (2000). *Modern analytical methods in art and archeology*. Wiley.
- Ciupiński, L., Fortuna-Zaleśna, E., Garbacz, H., Koss, A., Kurzydłowski, K. J., Marczak, J., Mróz, J., Onyszczyk, T., Rycyk, A., Sarzyński, A., Skrzeczanowski, W., Strzelec, M., Zatorska, A., & Żukowska, G. Z. (2010). Comparative laser spectroscopy diagnostics for ancient metallic artefacts exposed to environmental pollution. *Sensors*, 10, 4926–4949. <https://doi.org/10.3390/s100504926>
- Colomban, P. (2003). Polymerisation degree and Raman identification of ancient glasses used for jewellery, ceramics enamels and mosaics. *Journal of Non-Crystalline Solids*, 323, 180–187. [https://doi.org/10.1016/S0022-3093\(03\)00303-X](https://doi.org/10.1016/S0022-3093(03)00303-X)
- Colomban, P. (2004). Raman spectrometry, a unique tool to analyze and classify ancient ceramics and glasses. *Applied Physics A*, 79, 167–170. <https://doi.org/10.1007/s00339-004-2512-6>
- Colomban, P. (2005). Glasses, Glazes and Ceramics - Recognition of the Ancient Technology from the Raman Spectra. In H. G. M. Edwards & J. M. Chalmers (Eds.), *Raman spectroscopy in archaeology and art history* (pp. 192–206). Royal Society of Chemistry.
- Colomban, P., Etcheverry, M.-P., Asquier, M., Bounichou, M., & Tournié, A. (2006). Raman identification of ancient stained glasses and their degree of deterioration. *Journal of Raman Spectroscopy*, 37, 614–626. <https://doi.org/10.1002/jrs.1495>
- Colomban, P., Kirmizi, B., Zhao, B., Clais, J.-B., Yang, Y., & Droguet, V. (2020). Non-invasive on-site Raman study of pigments and glassy matrix of 17th–18th century painted enamelled Chinese metal wares: comparison with French enamelling technology. *Coatings*, 10, 471. <https://doi.org/10.3390/coatings10050471>
- Colomban, P., Tournié, A., & Bellot-Gurlet, L. (2006). Raman identification of glassy silicates used in ceramics, glass and jewellery: A tentative differentiation guide. *Journal of Raman Spectroscopy*, 37, 841–852. <https://doi.org/10.1002/jrs.1515>
- Conventi, A., Neri, E., & Verità, M. (2012). SEM-EDS analysis of ancient gold leaf glass mosaic tesserae. A contribution to the dating of the materials, IOP conference series. *Materials Science and Engineering*, 32, 012007. <https://doi.org/10.1088/1757-899X/32/1/012007>
- Edwards, H. G. M., & Chalmers, J. M. (2005). *Raman spectroscopy in archaeology and art history*. Royal Society of Chemistry.
- Franceschi, E. (2014). X-ray diffraction in cultural heritage and archaeology studies. *Open Access Library Journal*, 1, 1–10. <https://doi.org/10.4236/oalib.1100437>
- Freestone, I. C. (1994). Chemical analysis of “raw” glass fragments. In H. R. Hurst (Ed.), *Excavation of Chartage, Vol II. The Circular Harbour, North Side*. Oxford University Press.
- Frost, R. L., Čejka, J., Ayoko, G. A., & Dickfos, M. J. (2008). Raman spectroscopic study of the uranyl carbonate mineral voglite. *Journal of Raman Spectroscopy*, 39, 374–379. <https://doi.org/10.1002/jrs.1829>
- Galli, S., Mastelloni, M., Ponterio, R., Sabatino, G., & Triscari, M. (2004). Raman and scanning electron microscopy and energy dispersive x-ray techniques for the characterization of colouring and opaquening agents in Roman mosaic glass tesserae. *Journal of Raman Spectroscopy*, 35, 622–627. <https://doi.org/10.1002/jrs.1181>
- Garrison, E. (2014). X-Ray diffraction (XRD): applications in archaeology. In C. Smith (Ed.), *Encyclopedia of global archaeology* (p. 290). Springer. https://doi.org/10.1007/978-1-4419-0465-2_339
- Gates-Rector, S. D., & Blanton, T. N. (2019). The powder diffraction file: A quality materials characterization database. *Powder Diffraction*, 34, 352–360. <https://doi.org/10.1017/S0885715619000812>
- Georgiev, Z. (2018). The building Casino–Episcopal residence at Stobi, *International archaeological conference Between East and West: Stobi and the cities of the Roman provinces in the Balkans*, Stobi, 27–30 September 2018. *Studies in the Antiquities of Stobi*, Volume V.
- Goldsmith, J. R., Graf, D. L., Witters, J., & Northrop, D. A. (1962). Studies in the system $\text{CaCO}_3\cdot\text{MgCO}_3\cdot\text{FeCO}_3$: 1. Phase relations; 2. A method for major-element spectrochemical analysis; 3. Compositions of some ferroan dolomites. *Journal of Geology*, 70, 659–688. <https://doi.org/10.1086/626865>
- Gorin-Rosen, Y. (2015). Byzantine gold glass from excavations on the Holy Land. *Journal of Glass Studies*, 57, 97–120.
- Guo, Z., Yu, L., Tian, S., Lv, X., & Xue, W. (2020). Raman spectroscopy analysis of minerals based on feature visualization. *Spectroscopy*, 35, 37–46.
- Heaney, P. J., McKeown, D. A., & Post, J. E. (2007). Anomalous behavior at the *I2/a* to *Imab* phase transition in SiO_2 -moganite: An analysis using hard-mode Raman spectroscopy. *American Mineralogist*, 92, 631–639. <https://doi.org/10.2138/am.2007.2184>
- Henderson, J. (2013). *Ancient glass: An interdisciplinary exploration*. Cambridge University Press. <https://doi.org/10.1017/CBO9781139021883>
- Jawhari, T., Roid, A., & Casado, J. (1995). Raman spectroscopic characterization of some commercially available carbon black materials. *Carbon*, 33, 1561–1565. [https://doi.org/10.1016/0008-6223\(95\)00117-V](https://doi.org/10.1016/0008-6223(95)00117-V)
- Juhász, L., Moldován, K., Gurikov, P., Liebner, F., Fábrián, I., Kalmár, J., & Cserhádi, C. (2021). False morphology of aerogels caused by gold coating for SEM imaging. *Polyymers*, 13, 588–599. <https://doi.org/10.3390/polym13040588>
- Katičić, R. (1976). *Ancient languages of the Balkans* (p. 53). Mouton. <https://doi.org/10.1515/9783111568874>

- Kimmel, G., & Mogilyanski, D. (2009). Advantages and disadvantages of fast XRPD measurement by using image-plate and rotating anode source. *Zeitschrift für Kristallographie, Supplements*, 30, 171–176. <https://doi.org/10.1524/zksu.2009.0024>
- Knappett, C., Pirrie, D., Power, M., & Nikolakopoulou, I. (2011). Mineralogical analysis and provenancing of ancient ceramics using automated SEM-EDS analysis (QEMSCAN®): a pilot study on LB I pottery from Akrotiri, Thera. *Journal of Archaeological Science*, 38, 219–232. <https://doi.org/10.1016/j.jas.2010.08.022>
- Krishnamurti, D. (1956). Raman spectrum of magnesite. *Proceedings of the Indian Academy of Sciences–Section A*, 43, 210–212. <https://doi.org/10.1007/BF03052736>
- Krishnan, R. S. (1945). Raman spectrum of quartz. *Nature*, 155, 452. <https://doi.org/10.1038/155452a0>
- Kudin, K. N., Ozbas, B., Schniepp, H. C., Prud'homme, R. K., Aksay, I. A., & Car, R. (2008). Raman spectra of graphite oxide and functionalized graphene sheets. *Nano Letters*, 8, 36–41. <https://doi.org/10.1021/nl071822y>
- Kuisma-Kursula, P. (2000). Accuracy, precision and detection limits of SEM–WDS, SEM–EDS and PIXE in the multi-elemental analysis of medieval glass. *X-Ray Spectrometry*, 29, 111–118. [https://doi.org/10.1002/\(SICI\)1097-4539\(200001/02\)29:1<111::AID-XRS408>3.0.CO;2-W](https://doi.org/10.1002/(SICI)1097-4539(200001/02)29:1<111::AID-XRS408>3.0.CO;2-W)
- Ma, Y., Yan, W., Sun, Q., & Liu, X. (2021). Raman and infrared spectroscopic quantification of the carbonate concentration in K₂CO₃ aqueous solutions with water as an internal standard. *Geoscience Frontiers*, 12, 1018–1030. <https://doi.org/10.1016/j.gsf.2020.03.002>
- Madariaga, J. M., & Candeias, A. (2019). Applications of Raman spectroscopy in art and archeology. *Journal of Raman Spectroscopy*, 50, 137–142. <https://doi.org/10.1002/jrs.5571>
- Mäkie, P., Westin, G., Persson, P., & Österlund, L. (2011). Adsorption of trimethyl phosphate on maghemite, hematite, and goethite nanoparticles. *Journal of Physical Chemistry A*, 115, 8948–8959. <https://doi.org/10.1021/jp201065w>
- Mano-Zissi, D. (1973). Stratigraphic problems and the urban development of Stobi. In D. Mano-Zissi & J. Wiseman (Eds.), *Studies in the antiquities of Stobi* (Vol. I, pp. 187–224). Naucno Delo.
- Mano Zissi, G. (1940). The excavations in Stobi in the present year, Umetnichki Pregled, Book II, Belgrade. (in Serbian).
- Marshall, C. P., & Olcott Marshall, A. (2011). Hematite and carbonaceous materials in geological samples: A cautionary tale. *Spectrochimica Acta Part A*, 80, 133–137. <https://doi.org/10.1016/j.saa.2011.03.006>
- McMillan, P. F. (1989). Raman spectroscopy in mineralogy and geochemistry. *Annual Review of Earth and Planetary Sciences*, 17, 255–283. <https://doi.org/10.1146/annurev.earth.17.050189.001351>
- McMillan, P. F., & Hofmeister, A. (1988). Infrared and Raman spectroscopy. In F. C. Hawthorne (Ed.), *Spectroscopic methods in mineralogy and geology. Reviews in mineralogy* (Vol. 18, pp. 99–159). Mineralogical Society of America.
- Miriello, D., Antonelli, F., Apollaro, C., Bloise, A., Bruno, N., Catalano, M., Columbu, S., Crisci, G. M., De Luca, R., Lezzerini, M., Mancuso, S., & La Marca, A. (2015). A petro-chemical study of ancient mortars from the archaeological site of Kyeme (Turkey). *Periodico di Mineralogia*, 84(Spec. Iss), 497–517. <https://doi.org/10.2451/2015PM0028>
- Moon, D.-H., Kim, S.-J., Nam, S.-W., & Cho, H.-G. (2021). X-ray diffraction analysis of clay particles in ancient baekje black pottery: Indicator of the firing parameters. *Minerals*, 11, 1230. <https://doi.org/10.3390/min11111239>
- Nakai, I., & Abe, Y. (2012). Portable X-ray powder diffractometer for the analysis of art and archaeological materials. *Applied Physics A*, 106, 279–293. <https://doi.org/10.1007/s00339-011-6694-4>
- Nasdala, L., & Schmidt, C. (2020). Applications of Raman spectroscopy in mineralogy and geochemistry. *Elements*, 16, 99–104. <https://doi.org/10.2138/gselements.16.2.99>
- Ollier, N., Charpentier, T., Boizot, B., Wallez, G., & Ghaleb, D. (2004). A Raman and MAS NMR study of mixed alkali Na–K and Na–Li aluminoborosilicate glasses. *Journal of Non-Crystalline Solids*, 341, 26–34. <https://doi.org/10.1016/j.jnoncrysol.2004.05.010>
- Pawlyta, M., Rouzaud, J.-N., & Duber, S. (2015). Raman microspectroscopy characterization of carbon blacks: Spectral analysis and structural information. *Carbon*, 84, 479–490. <https://doi.org/10.1016/j.carbon.2014.12.030>
- Prinsloo, L. C., Wood, N., Loubser, M., Veryryn, S. M. C., & Tiley, S. (2005). Re-dating of Chinese celadon shards excavated on Mapungubwe Hill, a 13th century iron age site in South Africa, using Raman spectroscopy, XRF and XRD. *Journal of Raman Spectroscopy*, 36, 808–816. <https://doi.org/10.1002/jrs.1367>
- Reiche, I., Pages-Camagna, S., & Lambacher, L. (2004). In situ Raman spectroscopic investigations of the adorning gemstones on the reliquary Heinrich's Cross from the treasury of Basel Cathedral. *Journal of Raman Spectroscopy*, 35, 719–725. <https://doi.org/10.1002/jrs.1197>
- Robeva-Čukovska, L., Georgiev, Z., & Boev, B. (2008–2009). Research on the early Christian inlay work from the archaeological site Stobi. *Patrimonium.Mk*, 3-6, 233–238. (in Macedonian).
- Robinet, L., Bouquillon, A., & Hartwig, J. (2008). Correlations between Raman parameters and elemental composition in lead and lead alkali silicate glasses. *Journal of Raman Spectroscopy*, 39, 618–626. <https://doi.org/10.1002/jrs.1894>
- Roisman, J., & Worthington, I. (Eds.). (2010). *A companion to ancient Macedonia (Blackwell companions to the ancient world)*. Wiley-Blackwell.
- Rosenberg, P. E. (1991). Structural variation in the dolomite-ankerite solid-solution series: An X-ray, Mössbauer, and TEM study – Discussion. *American Mineralogist*, 76, 659–662.
- Rutt, H. N., & Nicola, J. H. (1974). Raman spectra of carbonates of calcite structure. *Journal of Physics C*, 7, 4522–4528. <https://doi.org/10.1088/0022-3719/7/24/015>
- Schreiner, M., Frühmann, B., Jembrih-Simbürger, D., & Linke, R. (2004). X-rays in art and archeology: An overview. *Powder Diffraction*, 19, 3–11. <https://doi.org/10.1154/1.1649963>

- Spivak, A., Solopova, N., Cerantola, V., Bykova, E., Zakharchenko, E., Dubrovinsky, L., & Litvin, Y. (2014). Raman study of MgCO_3 – FeCO_3 carbonate solid solution at high pressures up to 55 Gpa. *Physics and Chemistry of Minerals*, 41, 633–638. <https://doi.org/10.1007/s00269-014-0676-y>
- Tuinstra, R., & Koenig, J. L. (1970). Raman spectrum of graphite. *Journal of Chemical Physics*, 53, 1126–1130. <https://doi.org/10.1063/1.1674108>
- Tykot, R. H. (2004). Scientific methods and applications to archeological provenance studies. In M. Martini, M. Milazzo, & M. Piacentini (Eds.), *International school of physics "Enrico Fermi"* (pp. 407–432). Course CLIV, IOS Press.
- Valderrama, D. M. A., Cuaspid, J. A. G., Roether, J. A., & Boccaccini, A. R. (2019). Development and characterization of glass-ceramics from combinations of slag, fly ash, and glass cullet without adding nucleating agents. *Materials*, 12, 2032. <https://doi.org/10.3390/ma12122032>
- Veblen, D. R., & Post, J. E. (1983). A TEM study of fibrous cuprite (chalcotrichite); microstructures and growth mechanisms. *American Mineralogist*, 68, 790–803.
- Wiseman, J. (1973). *Stobi, A guide to the excavations*. Belgrade: Beograd.
- Wiseman, J. (2007). Environmental deterioration and human agency in ancient Macedonia: a case study. *Geoarchaeology: An International Journal*, 22, 85–110. <https://doi.org/10.1002/gea.20148>

SUPPORTING INFORMATION

Additional supporting information can be found online in the Supporting Information section at the end of this article.

How to cite this article: Makreski, P., Šijakova-Ivanova, T., Georgiev, Z., Balabanova Aleksova, D., Reka, A. A., Boev, B., & Jovanovski, G. (2022). The restored opus sectile panel from the luxurious episcopal residence in the ancient city of Stobi—mineralogical and chemical findings. *Archaeometry*, 1–17. <https://doi.org/10.1111/arcm.12834>